J. Fluid Mech. (1997), *vol.* 347, *pp.* 289–314. Printed in the United Kingdom

Turbulent plane Couette flow subject to strong system rotation

By KNUT H. BECH AND HELGE I. ANDERSSON

Division of Applied Mechanics, The Norwegian University of Science and Technology, N-7034 Trondheim, Norway

(Received 4 July 1996 and in revised form 24 April 1997)

System rotation is known to substantially affect the mean flow pattern as well as the turbulence structure in rotating channel flows. In a numerical study of plane Couette flow rotating slowly about an axis aligned with the mean vorticity, Bech & Andersson (1996*a*) found that the turbulence level was damped in the presence of anticyclonic system rotation, in spite of the occurrence of longitudinal counter-rotating roll cells. Moreover, the turbulence anisotropy was practically unaffected by the weak rotation, for which the rotation number Ro, defined as the ratio of twice the imposed angular vorticity Ω to the shear rate of the corresponding laminar flow, was ± 0.01. The aim of the present paper is to explore the effects of stronger anticyclonic system rotation on directly simulated turbulent plane Couette flow. Turbulence statistics like energy, enstrophy and Taylor lengthscales, both componental and directional, were computed from the statistically steady flow fields and supplemented by structural information obtained by conditional sampling.

The designation of the imposed system rotation as 'high' was associated with a reversal of the conventional Reynolds stress anisotropy so that the velocity fluctuations perpendicular to the wall exceeded those in the streamwise direction. It was observed that the anisotropy reversal was accompanied by an appreciable region of the mean velocity profile with slope $\sim 2\Omega$, i.e. the absolute mean vorticity tended to zero. It is particularly noteworthy that these characteristic features were shared by two fundamentally different flow regimes. First, the two-dimensional roll cell pattern already observed at $Ro = 0.01$ became more regular and energetic at $Ro = 0.10$ and 0.20, whereas the turbulence level was reduced by about 50%. Then, when Ro was further increased to 0.50, a disordering of the predominant roll cell pattern set in during a transient period until the flow field settled at a new statistically steady state substantially less affected by the roll cells. This was accompanied by a substantial amplification of the streamwise turbulent vorticity and an anomalous variation of the mean turbulent kinetic energy which peaked in the middle of the channel rather than near the walls. While the predominant flow structures of the non-rotating flow were longitudinal streaks, system rotation generated streamwise vortices, either ordered secondary flow or quasi-streamwise vortices. Eventually, at $Ro = 1.0$, the turbulent fluctuations were completely suppressed and the flow field relaminarized.

1. Introduction

As shown in our previous paper on *weakly* rotating turbulent plane Couette flow (Bech & Andersson 1996*a*, hereafter referred to as BA), this flow case is particularly well suited for the study of the Coriolis instability in turbulent channel flow. The

constant sign of the mean vorticity distribution makes the destabilizing (stabilizing) effects symmetric with respect to the centreline, thereby simplifying the interpretation of the observed changes in turbulence structure due to system rotation, as compared to the pressure-driven Poiseuille flow in which the mean vorticity inevitably changes its sign. Here, we will focus on the destabilized flow where the Coriolis acceleration is sufficiently strong to impose significant changes in the turbulence anisotropy. Particular efforts will be made to distinguish between turbulence and the secondary flow induced by the system rotation, thereby obtaining more detailed physical information than what has so far been derived from experimental and numerical investigations of the plane Poiseuille flow (Johnston, Halleen & Lezius 1972; Kristoffersen & Andersson 1993; Andersson & Kristoffersen 1995; Nakabayashi & Kitoh 1996, Lamballais, Lesieur & Metais 1996*a*, *b*).

The kinetic energy of the fluctuating flow field is usually used to quantify the degree of destabilization. Both secondary flow, which does not contribute to the volume flow, and turbulence are considered as fluctuations about the mean, or primary flow. If the kinetic energy of the fluctuations is increased by increasing the rate of system rotation, then the flow is categorized as destabilized. If the fluctuating flow field becomes less energetic by increasing the rotation rate further, the flow field is classified as restabilized. The ultimate state of restabilization is the case where both secondary flow and turbulence vanish. According to the Taylor–Proudman theorem, this state of total restabilization occurs at infinite rotation rate, see e.g. Greenspan (1968).

Previous studies of the effect of system rotation on turbulence in shear flows have sometimes postulated a close relationship between the stability characteristics of the mean flow, or even laminar flow, and the amplification and damping of turbulence, see Tritton (1992). As was shown by BA however, the onset of the roll cell instability may actually lead to damping of the turbulence in plane Couette flow. In experimental investigations it is difficult to obtain quantitative results simultaneously for secondary flow and turbulence because the roll cells are not completely steady. Thus numerical simulations are a feasible source of quantitative results.

For the plane Poiseuille case, Kristoffersen & Andersson (1993) observed that there was a significant increase in the kinetic energy of the fluctuating field in the destabilized wall layer when the rotation rate was increased from zero to a relatively low level, a phenomenon which can be ascribed to the onset of the roll cell instability. At the highest rotation rate considered by Kristoffersen & Andersson, the wall shear stress was reduced, thereby indicating a restabilization of the flow. In the studies of the rotating turbulent Poiseuille flow by Johnston *et al.* (1972) and Kristoffersen & Andersson (1993), it was observed that a portion of the anticyclonic (destabilized) region exhibited approximately zero absolute mean vorticity, i.e. the vorticity in the inertial frame was zero so that $2\Omega - \partial U/\partial y = 0$. Here, 2Ω is twice the angular velocity of the reference system in the spanwise z-direction, U is the mean velocity in the x-direction, while y is the wall-normal direction so that $-\partial U/\partial y$ is the vorticity of the mean flow in the rotating reference frame. The observed zero absolute vorticity is physically plausible because it is easy to imagine that the mean rotation of fluid particles in the inertial frame is zero. The physical origin of this phenomenon is somewhat unclear. It is not observed in laminar flow but it was, however, observed in the inviscid region between the developing boundary layers in the entrance of a rotating channel by Koyama & Ohuchi (1985). In this case it is just an example of potential flow, but it is notable that roll cells were observed. In an anticyclonic mixing layer with destabilization due to system rotation, Metais *et al.* (1995) observed

a region of approximately zero absolute vorticity. The Kelvin–Helmholtz vortices were suppressed, and instead quasi-streamwise vortices were observed. In two recent papers, Lamballais *et al.* (1996*a*, *b*) investigated the effect of system rotation on coherent vortices in simulated plane Poiseuille flow. A remarkable ordering of quasi-streamwise vortices was observed in the destabilized layer, together with a region of approximately zero absolute vorticity away from the wall. The ordered vortices were more parallel to the streamwise axis than in the non-rotating case.

Several theoretical approaches have been proposed in order to give criteria for the occurrence of destabilization. A review of some of these approaches was given by Tritton (1992). The commonly accepted criterion for instability in rotating shear flows is that the dimensionless parameter

$$S = \frac{2\Omega}{-\partial U/\partial y} \tag{1.1}$$

should be in the interval $(-1, 0)$, which states that instability occurs for anticyclonic rotation that is not too strong. In fully developed turbulent channel flow, however, destabilized regions with $S < -1$ have been observed by Andersson & Kristoffersen (1995).

It can further be demonstrated that maximum destabilization occurs when $S = -\frac{1}{2}$. This is the so-called Bradshaw–Richardson criterion, which was originally derived by Bradshaw (1969). It can also be obtained from the simplified Reynolds stress equation scheme (SRSE) introduced by Johnston *et al.* (1972) and further developed by Tritton (1992). This approach makes no distinction between secondary flow and turbulence, so one should be careful not to draw firm conclusions on the stability characteristics of turbulence alone. The Bradshaw–Richardson criterion for maximum destabilization has also been demonstrated by Cambon *et al.* (1994) using linear stability analysis and numerical simulations of flows where large-scale vortices are superimposed on weak turbulence. In this case, the denominator in (1.1) was replaced by the spanwise r.m.s. vorticity of the large-scale structures. Lesieur, Yanase & Metais (1991) and Metais *et al.* (1992) considered the effect of background vorticity on initially two-dimensional coherent structures using linear theory and numerical simulation. It was suggested that maximum destabilization occurs around zero absolute vorticity. They further reported that slight anticyclonic rotation is destabilizing, but becomes stabilizing at higher rotation rates. One should bear in mind, however, that various authors use different definitions of the mean vorticity, and thus of the S-parameter. The degree of stabilization or destabilization is dependent on the scale of motion under consideration, and also the initial conditions. The Bradshaw–Richardson criterion is not very meaningful for the case of steady channel flow, where the destabilized wall layer exhibits low magnitude of S, whereas the S-value in the central region is close to -1 (see e.g. Andersson & Kristoffersen 1995). The problem can be circumvented by using a value of $-\partial U/\partial y$ from the corresponding non-rotating turbulent flow, or even $-U_w/h$ (U_w being wall velocity) for laminar plane Couette flow. Maximum destabilization of laminar rotating Couette flow occurs at $S = -\frac{1}{2}$ (at $Re = 21$, see Hart 1971), and the flow is unstable when $-1 < S < 0$.

Bartello, Metais & Lesieur (1994) observed that system rotation created vortex asymmetry in homogeneous turbulence. Around zero absolute vorticity, anticyclonic two-dimensional structures were stretched in the longitudinal direction while the cyclonic structures were stable. This is somewhat analogous to the longitudinal roll cells observed on the anticyclonic side of Poiseuille flow. Bartello *et al.* also reported on the decay of homogeneous turbulence in a rotating frame. With approximately

zero absolute vorticity, they found that the energy associated with two-dimensional motion decayed more slowly than the energy of the three-dimensional modes. Bidokhti & Tritton (1992) performed a detailed experimental study of a rotating free shear layer, in which the mean shear maintains the same sign throughout the flow. The Kelvin–Helmholtz instability was found to be suppressed by anticyclonic rotation, but Bidokhti & Tritton did not observe secondary, or coherent, streamwise vortices. They found that the Reynolds stress in the direction normal to the rotation axis and the mean flow exceeded the streamwise stress component with strong anticyclonic rotation. Restabilization was observed with even stronger anticyclonic rotation.

Recently, Tillmark & Alfredsson (1996) published experimental results on laminar and turbulent rotating plane Couette flow. In the turbulent case (Reynolds number $Re = 700$, rotation number $Ro = 0.1$), regular roll cells were observed in the visualizations, becoming more pronounced as the rotation rate was increased. (At this Reynolds number, the maximum rotation number of the experimental apparatus was approximately 0.12.) At $Ro = 0.01$ and $Re = 200$, the roll cells were first observed to be approximately steady, then a wavy instability was observed, culminating in breakdown and regeneration of steady roll cells. Secondary and tertiary instabilities of the differentially heated (laminar) Couette flow have been investigated by Clever & Busse (1992). As was shown by Hart (1971), this problem is analogous to the rotating plane Couette flow problem in the case of streamwise-independent disturbances. Thus the secondary and tertiary instabilities found by Clever & Busse, exhibiting waviness in the streamwise direction, are not directly analogous to the rotating Couette flow problem, but one might expect to find similarities. The numerical simulations by Domaradzki & Metcalfe (1988) of the differentially heated plane Couette flow at relatively high Rayleigh numbers showed streamwise organized structures. For moderate Rayleigh numbers, the motion was organized with a low turbulence intensity. The organized flow was able to increase the heat transfer compared to the less organized. At higher Rayleigh numbers, the flow appeared more disorganized, thus decreasing the heat transfer. Komminaho, Lundbladh & Johansson (1996) performed simulations of the turbulent plane Couette subject to stabilizing rotation, and observed that the flow relaminarized at $Ro = -0.060$ for a Reynolds number of 750.

Some of the important results that seem to be common to several different rotating turbulent shear flows can be summarized as follows.

Destabilization occurs for anticyclonic rotation that is not too strong. There seems to be a close correspondence between laminar and turbulent flow in this respect.

For significant anticyclonic rotation rates, a region of zero absolute vorticity can be observed away from solid walls.

The destabilizing system rotation tends to generate streamwise vortices. These vortices can in some cases be similar to the linear Coriolis instability of the laminar flow.

The turbulence anisotropy is reversed by significant destabilizing rotation, so that the cross-stream or wall-normal turbulent stress is enhanced and the streamwise stress component is inhibited.

In this paper we will examine the effects of strong system rotation on turbulent plane Couette flow. The precise meaning of the term 'strong rotation' will be defined in the next section. Our information is gathered from direct numerical simulations of the plane Couette flow at different rotation numbers, so that the system rotation is anticyclonic, and is in most cases destabilizing. The present contribution is a continuation of our previous paper (BA), where the formation of the roll cells and

their relation to turbulence at a low rotation rate was discussed. Here, we proceed to higher, destabilizing rotation rates.

2. Strong rotation

We express the dimensionless background vorticity, or rotation number, as $Ro = 2\Omega h/U_w$, where U_w is the prescribed wall velocity. In our flow configuration (see BA for a sketch), the upper wall at $y = h$ moves with velocity $U = U_w$, while the lower wall at $y = -h$ moves with $-U_w$. The dynamics of the flow are affected by the difference between the wall velocities, and in the case of system rotation also by the sign of the absolute vorticity. The Reynolds number is defined as $Re = U_w h/\nu$, where ν is the kinematic viscosity of the incompressible fluid. In flows with roll-cell instabilities, it is convenient to decompose the instantaneous velocity and pressure fields into three components so that $u_i'(x, y, z, t) = U_i(y) + \widetilde{u}_i(y, z) + u_i(x, y, z, t)$, see BA. In cases where the secondary flow $\widetilde{u}_i(y, z)$ contains significant kinetic energy as compared to turbulence $u_i(x, y, z, t)$, and the two-point correlations contain laminar-like modes, the secondary flow is referred to as roll cells. The secondary flow will also be classified as two-dimensional, because of its independence of the x-direction. The following notation will apply for the averaging and decomposition of the velocity field. The average of ϕ with respect to time and the x-direction is denoted by $\overline{\phi}$. (The turbulence is assumed to be homogeneous in the x-direction and time.) Other spatial averages are denoted by $\langle\phi\rangle_\eta$ where the subscript signifies averaging along the η-axis. We use $k = \frac{1}{2}\langle\overline{u_j u_j}\rangle_z$ for the kinetic energy of the turbulence.

The averaged streamwise momentum equation (see BA) yields that the total shear stress is constant and positive throughout the flow. Here, we note that the sum of the turbulent shear stress $-\langle\overline{uv}\rangle_z$ and the apparent shear stress $-\langle\widetilde{u}\widetilde{v}\rangle_z$ is positive, i.e.

$$-\sigma_{12} = -\langle\overline{uv} + \widetilde{u}\widetilde{v}\rangle_z > 0, \tag{2.1}$$

where σ_{12} is defined as $\langle\overline{(u_i + \widetilde{u}_i)(u_j + \widetilde{u}_j)}\rangle_z$.

Consider the stress anisotropy measured by the parameter $a = \sigma_{22}/\sigma_{11} - 1$. We define strong rotation as a case in which $a > 0$ so that $\sigma_{22} > \sigma_{11}$. For this argument, we need the transport equations for the stresses σ_{ij}, applied in the SRSE scheme of Johnston *et al.* (1972) and Tritton (1992). If $a > 0$, the sum of the mean shear and rotational production terms in the transport equation for $\sigma_{22} - \sigma_{11}$ is positive, i.e.

$$-2\sigma_{12}\left(4\Omega - \frac{\partial U}{\partial y}\right) > 0. \tag{2.2}$$

Now $-\sigma_{12} > 0$ from (2.1) and (2.2) thus implies that $S < -\frac{1}{2}$. It must also be required that the total production of $-\sigma_{12}$ is greater than zero, i.e.

$$\sigma_{11}\left[\frac{\partial U}{\partial y} - a\left(2\Omega - \frac{\partial U}{\partial y}\right)\right] > 0. \tag{2.3}$$

In the present case where $\partial U/\partial y > 0$ throughout the channel, this occurs when $S > -(1 + 1/a)$. It is anticipated that the terms involving pressure act as sinks for $-\sigma_{12}$ as they do in the non-rotating case, see Bech & Andersson (1996*b*). In the case of (2.2), the pressure–strain term $\phi_{22} - \phi_{11}$ is expected to be a sink term. Because σ_{22} is larger than σ_{11} and σ_{33}, it can be assumed that $\phi_{22} - \phi_{11} = -(2\phi_{11} + \phi_{33})$ is less than zero.

Ro	Re_τ	Re_t	$T_{s,1}$	$T_{s,2}$
0.0	82.2	142.4	16.4	1.8
0.1	106.7	97.6	3.4	3.4
0.2	107.2	103.0	8.0	0
0.5	91.0	180.9	6.6	3.9

TABLE 1. DNS presented in this paper. The $Ro = 0$ simulation was described in Bech *et al.* (1995). The sampling time for the statistics ($T_{s,1}$) and fields ($T_{s,2}$) databases are given in h/u_τ.

One could alternatively use the equation for σ_{11} and show that $S > -1$ for the total production of σ_{11} to be positive, see for example Johnston *et al.* (1972). This is, however, not strictly correct in the case of strong rotation, because in that case, the pressure–strain correlation becomes a significant source term for σ_{11}.

In summary, for unstable strong rotation

$$-\left(1+\frac{1}{a}\right) < S < -\tfrac{1}{2}. \tag{2.4}$$

where $a > 0$. The requirement (2.4) is different from previous findings in that (i) only strong rotation has been considered, (ii) the lower limit is a weaker formulation than the conventional criterion $S > -1$, and (iii) S is excluded from the upper half of the commonly accepted interval $(-1, 0)$.

3. Numerical simulations and conditional sampling

The direct numerical simulations (DNS) presented in this paper (see table 1) were run with the ECCLES code developed by Gavrilakis *et al.* (1986). The technical details of the computations with imposed system rotation did not differ significantly from the simulation of the non-rotating Couette flow, which was described by Bech *et al.* (1995). The Reynolds number based on wall velocity and half-channel width was $Re = 1300$. The computational domain was $10\pi h \times 2h \times 4\pi h$ in the x-, y- and z-directions, respectively. The number of grid points was $256 \times 70 \times 256$ in all simulations. For simulations with $Ro \geqslant 0.1$, the inhomogeneous distribution of grid points in the wall-normal direction was somewhat changed, thereby moving the first grid point from $y^+ = 0.36$ ($Ro = 0$) to $y^+ = 0.27$.

The results presented in §4 were taken from two kinds of databases: the statistics database, which consisted of time- and space-averaged quantities, and a database of samples of the instantaneous flow field (u, v, w, p), i.e. the fields database. In the latter case, six samples separated by a constant time interval were considered at each rotation number. The fields database for $Ro = 0.2$ was an exception because only one dump was recorded. As will be seen from table 1, different sampling times were applied for the different Ro. A detection method similar to that described by Guezennec, Piomelli & Kim (1989) was applied to study the influence of system rotation on near-wall turbulence-generating events. The quadrant detection scheme, which should be familiar to many readers, triggers on events with a strong positive correlation $-uv$ and sorts the events into quadrant 2 (Q2, $u < 0, v > 0$) and quadrant 4 (Q4, $u > 0, v < 0$). Guezennec *et al.* utilized the observation that near-wall turbulence-generating events usually are detected together with streamwise vortices. This is so even though the vorticity is not used in the detection algorithm, see for example Bech *et al.* (1995). The special feature of the method suggested by Guezennec *et al.* is that

the circulation, along a path in the cross-stream plane enclosing possible streamwise vortices, is calculated for each individual event. The sign of the circulation is then utilized to decide whether the event should be mirrored in the (x, y)-plane before it is included in the ensemble average. In this way, the asymmetry of the individual events is preserved in the ensemble average. Without this precaution, the ensemble average will show approximately symmetric pairs of counter-rotating vortices.

Here, the detection was carried out at the position where $\langle\overline{u^2}\rangle_z$ attained its near-wall maximum, and the detection criterion was $uv/\langle uv\rangle_{xz} \geqslant 7.5$, i.e. based on the instantaneous plane average of the turbulent Reynolds shear stress. For the non-rotating case, this criterion gave the same number of events as that applied by Guezennec *et al.*, i.e. $-uv/u_{r.m.s.}v_{r.m.s.} \geqslant 3.5$. For the cases with rotation, the equivalent limits using their criterion would have been 3 ($Ro = 0.1$) and 4.5 ($Ro = 0.5$). To study whether events near one wall influenced the flow adjacent to the other wall, the detection was done exclusively near the lower wall at $y = -1$, while the ensemble averages extended from $y = -1$ to $y = 1$. The detection and conditional sampling were carried out on the fields database.

4. Results

In the following subsections, the effect of system rotation will be studied from various points of view. The second subsection is devoted to the study of lengthscales, while the third subsection treats the changes in the anisotropy of the Reynolds stresses and the vorticity induced by rotation. In the last subsection, the effect of Coriolis acceleration on turbulence-generating events in the near-wall region will be examined through visualization and a qualitative discussion. In the following, x-, y- and z-axes will be scaled by h, mean velocity by U_w, vorticity by U_w/h and kinetic energies and Reynolds stresses by the square of the friction velocity at zero rotation rate ($u_{\tau,0}$). To provide the reader with a concrete idea of the magnitude of system rotation encountered in this study, we refer to the plane Couette flow apparatus by Tillmark & Alfredsson (1996). With water as medium and $h = 1$ cm, a rotation number $Ro = 0.1$ would correspond to approximately 6 r.p.m. at $Re = 1300$. In this apparatus, $Ro = 0.1$ can be obtained up to Reynolds numbers of approximately 800.

4.1. *Primary effects of system rotation*

Figure 1 shows the change of the mean velocity profile $U(y)$ due to system rotation. The most apparent effect was the change of the mean shear, as well as its approximate constancy, in a wide region away from the walls. Using the solid curve corresponding to $Ro = 0$ as a reference, it is observed that system rotation makes the mean shear smaller or larger, depending on the magnitude of the background vorticity. This is better understood when one considers the absolute vorticity, or almost equivalently the parameter S which is displayed in figure 2(a). Zero absolute vorticity corresponds to $S = -1$. It is readily observed that S is within approximately 10% of -1.0 in a wide region of the flow, a region that is conveniently referred to as 'the central region'. The width of this core region, which extends from about $y = -0.5$ to $y = 0.5$ at $Ro = 0.1$, increased with increasing rotation number. The anisotropy parameter a is plotted in figure 2(b). There seems to be a correlation between the width of the regions with $S \simeq -1$ and $a > 0$ for $Ro = 0.2$ and 0.5, while the corresponding curves for $Ro = 0.1$ do not coincide in the same way. Results for $Ro = 0.01$, already treated in BA, were included in figure 2 to demonstrate the difference between weak and strong rotation. In the case of weak rotation $a < 0$, so that the anisotropy of the

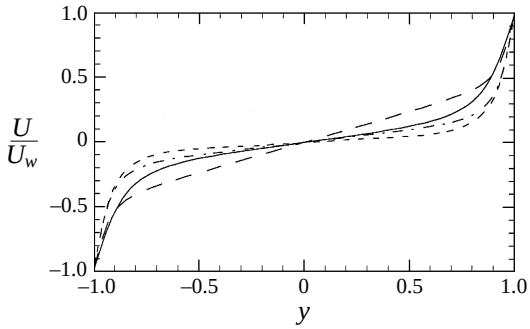

FIGURE 1. Mean velocity: —, $Ro = 0$; - - -, $Ro = 0.1$; — - —, $Ro = 0.2$; — — —, $Ro = 0.5$.

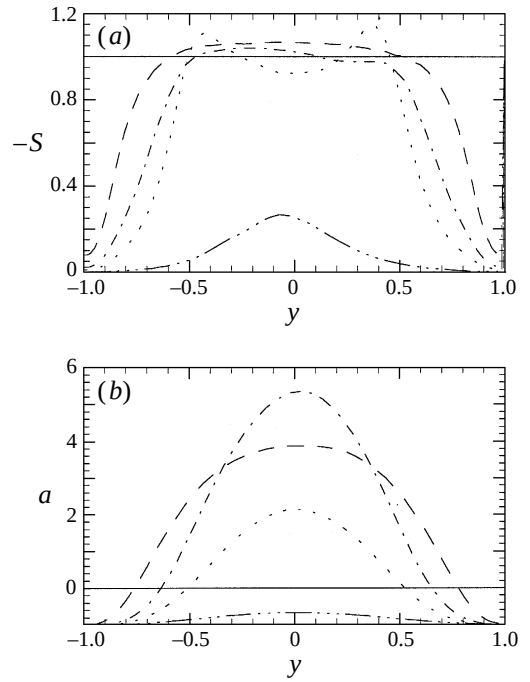

FIGURE 2. (*a*) The vorticity ratio S. (*b*) The anisotropy parameter a. — - - - —, $Ro = 0.01$; the other curves as in figure 1 except the solid lines which represent $S = -1$ and $a = 0$, respectively.

stresses was qualitatively the same as in the non-rotating case. $|S|$ was small and did not approach the salient value of 1.

Figure 1 shows that the near-wall regions with high shear were thinner, and that the wall shear stress was higher, in the cases with $Ro = 0.1$ and 0.2. The intermediate region, in which the mean shear changes most rapidly, was also influenced significantly by the changes in mean vorticity in the central region. As will be apparent in the following, the changing distribution of the mean velocity was accompanied by substantial alterations in the structure of the fluctuating flow field, both in the sense of secondary motion and the preferred directions of turbulent motions.

In the cases with $Ro = 0.1$ and 0.2, roll cells were a predominant feature of the flow field. Streamlines for the former case, obtained as a projection of the secondary flow in the (y, z)-plane, are depicted in figure 3. Hence, this motion is referred to as the

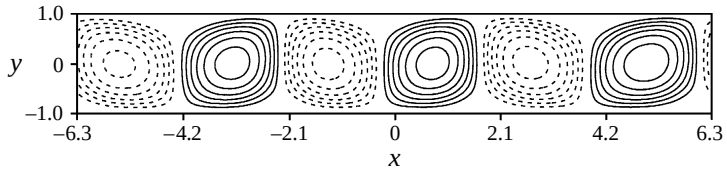

FIGURE 3. Stream function in the cross-flow plane derived from the secondary velocity field, $Ro = 0.1$. Contour increment $= 0.02U_w h$, broken lines are negative.

Ro	$\frac{1}{2}\langle\widetilde{v}^2 + \widetilde{w}^2\rangle_{yz}/\langle k_{tot}\rangle_y$	$\frac{1}{2}\langle\widetilde{u}^2\rangle_{yz}/\langle k_{tot}\rangle_y$	$\frac{1}{2}\langle\widetilde{v}^2 + \widetilde{w}^2\rangle_{yz}/\langle k_{c,tot}\rangle_y$
0.01	0.034	0.30	0.12
0.10	0.49	0.32	0.86
0.15†			0.25

† Data from Poiseuille flow simulation by Kristoffersen & Andersson (1993).

TABLE 2. Kinetic energy of cross-flow and streamwise secondary flow at different rotation rates. Here, $\langle k_{tot}\rangle_y = \frac{1}{2}\langle\widetilde{u}_j\widetilde{u}_j + \overline{u_j u_j}\rangle_{yz}$, $j = 1, 2, 3$ and $\langle k_{c,tot}\rangle_y$ is an abbreviation for the total energy of the motion in the cross-sectional plane, so that summation should be carried out over $j = 2, 3$ only.

cross-flow. Cross-flow patterns at some other rotation rates were presented by Bech & Andersson (1996*c*). The relative magnitude of the cross-flow energy increased by one order of magnitude when Ro was increased from 0.01 to 0.1, as can be observed from the second column in table 2, where we have made a comparison between roll-cell data from Couette and Poiseuille flow. The third column shows that the magnitude of the streamwise variations associated with the roll-cell mixing reached a 'saturation' level at weak rotation, while the cross-flow energy increased with increasing Ro. This behaviour is plausible because the Coriolis acceleration redirects streamwise momentum into the wall-normal direction.

The roll cells were more intense in the Couette flow case than in the Poiseuille flow, cf. table 2. There are several possible reasons for this. For example, the aspect ratio was not optimized, in the sense of filling the cross-section with persistent secondary vortices, in the Poiseuille flow simulation. Moreover, the rotation numbers did not necessarily correspond to the same degree of destabilization. However, Kristoffersen & Andersson (1993) remarked that the rotation number 0.15 gave relatively stable roll cells. Their results did also show that this rotation number gave rise to maximum total wall shear stress, which at least in Couette flow corresponds to maximum secondary kinetic energy. Finally, their results showed that the total kinetic energy was relatively large at this rotation rate. We therefore assume that it is reasonable to compare the cross-flow kinetic energies of the two lower rows in table 2, which implies that the roll cell instability is significantly stronger in the Couette flow as compared to the Poiseuille flow, and that the response of the two flows to rotation is different due to the differences in the symmetry of the mean vorticity.

The Reynolds numbers based on friction velocity were listed in table 1. Re_τ increased from zero rotation up to $Ro = 0.2$. The wall shear stress increased by 6% when Ro was increased from zero to 0.01, while the difference in τ_w between zero rotation and $Ro = 0.1$ was 68%. The effect of rotation is about 10 times greater at $Ro = 0.1$ than at $Ro = 0.01$. This is consistent with the tenfold intensification of the cross-flow as the rotation number is increased from 0.01 to 0.1, cf. table 2. Returning to the

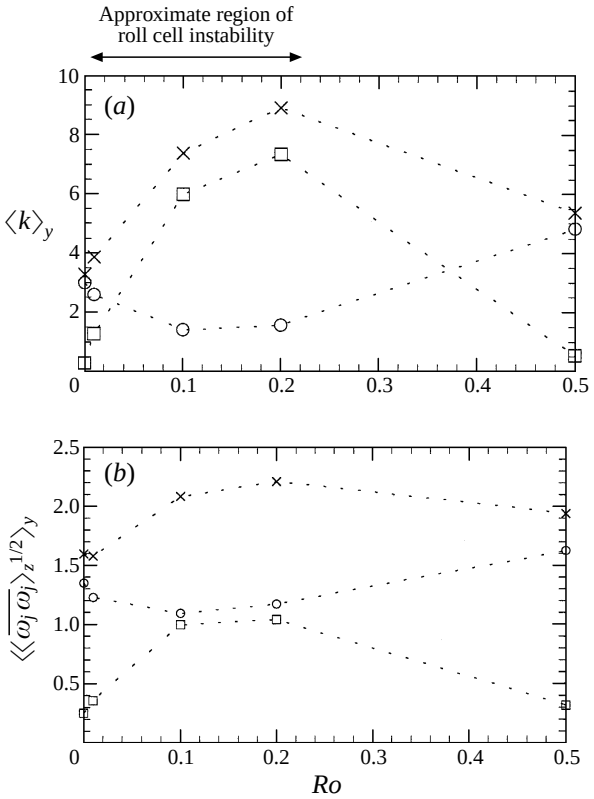

FIGURE 4. Volume and time-averaged (*a*) kinetic energies and (*b*) r.m.s. vorticity $\langle\langle \overline{\omega_j \omega_j} \rangle_z^{1/2} \rangle_y$. ○, turbulent; □, secondary; ×, total. Data from the $Ro = 0.01$ simulation by BA are included.

streamline topology in figure 3, it is seen that the streamlines were asymmetric with respect to $y = 0$. The solid contours represent positive values of the stream function, i.e. the motion is clockwise, and the dotted contours denote counter-clockwise flow. The density of streamlines is higher where fluid leaves the near-wall region than in the stagnation regions in which fluid approaches the wall. This behaviour is somewhat similar to that observed in Poiseuille flow by Kristoffersen & Andersson (1993), while it is more complex than that observed in weakly rotating Couette flow (BA).

In figure 4, overall effects of system rotation on kinetic energy and r.m.s. vorticity are summarized. Note that the dotted lines between the data points are not representative of the actual behaviour, but they were included to aid the visual interpretation of the figure. The volume-averaged kinetic energies ($\langle \widetilde{k} \rangle_y = \frac{1}{2} \langle \widetilde{u}_j \widetilde{u}_j \rangle_{yz}$ for the secondary flow) in figure 4(*a*) show how the flow is destabilized when Ro is increased from zero to 0.2. The sum $\langle k + \tilde{k} \rangle_y$ was 2.7 times larger at $Ro = 0.2$ compared to zero rotation. Note that the sum of the turbulent and secondary kinetic energies was exact to the accuracy of the direct simulation, while the partition between the two was somewhat influenced by the finite length of the computational box, as discussed in BA. However, there is no doubt that the increase of kinetic energy in the destabilized flow was due to the ordered secondary motion in the roll cells. The damping of turbulence, as already observed by BA at $Ro = 0.01$, was even more pronounced at $Ro \sim 0.1$. At $Ro = 0.2$, the contribution of the turbulent component to the total kinetic energy was only 18%.

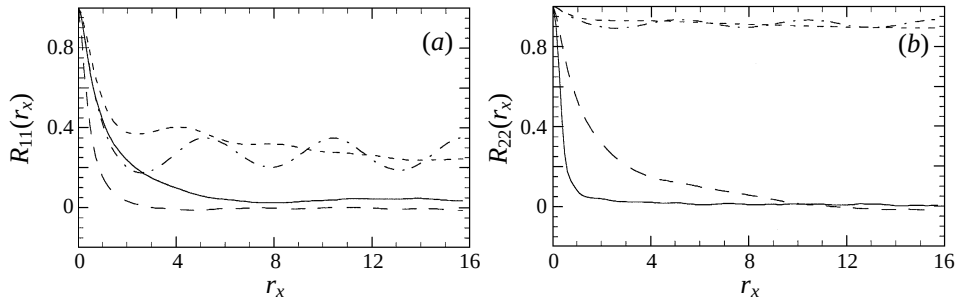

FIGURE 5. Streamwise two-point correlations of (*a*) $u+\widetilde{u}$ and (*b*) $v+\widetilde{v}$ at $y=0$. Legend as in figure 1. The abscissae is scaled by *h*.

We chose to plot the dimensionless r.m.s. vorticity, i.e. $\langle\overline{\omega_j\omega_j}\rangle_z^{1/2}$ for the turbulent component, because its magnitude is directly comparable with the rotation number or the vorticity of the laminar flow (which is 1 in the non-dimensional form applied here). In figure 4(*b*), the average over the *y*-direction is shown. The sum of the turbulent and secondary r.m.s. vorticity behaves qualitatively similarly to $\langle k+\tilde{k}\rangle_y$, except in the case of weak rotation ($Ro=0.01$) in which the damping of turbulence leads to an overall reduction of r.m.s. vorticity. At higher rotation rates up to 0.2, the total r.m.s. vorticity increases because the enhancement of the secondary vorticity is more significant than the damping of the turbulent vorticity. It is also observed that the secondary motion of the roll cells is relatively energetic, but contains less vorticity, compared to the turbulent motion. This difference is obviously due to the large lengthscale of the roll cells as compared to the dissipative turbulent eddies.

It is noteworthy that maximum destabilization occurred at a rotation number close to the magnitude of the mean centreline vorticity at $Ro=0$, namely $|-\partial U/\partial y|=0.22$. At higher rotation rates, the structure of the flow was observed to change. This is readily seen in figure 4(*a*), and to some lesser extent in 4(*b*). The secondary flow component was damped due to the disappearance of the steady roll cells. Even though the turbulence intensity increased significantly, the disappearance of the roll cells was associated with restabilization as both kinetic energy and r.m.s. vorticity (enstrophy) decreased. The concepts of destabilizing and restabilizing rotation are somewhat ambiguous here, because maximum destabilizing of the flow corresponds to maximum stabilization of turbulence, while restabilization of the flow corresponds to destabilization of turbulence. Maximum damping of turbulence, i.e. relaminarization, was observed at $Ro=1.0$. This is not shown in the figures, and the relaminarization could equally well have occurred at a somewhat lower rotation rate.

4.2. *Lengthscales*

Centreline values of the two-point velocity correlations

$$R_{jk}\left(r_{x_i}\right)=\overline{\left(\frac{\langle[u_j(t,\boldsymbol{x})+\widetilde{u}_j(\boldsymbol{x})][u_k(t,\boldsymbol{x}+r_{x_i})+\widetilde{u}_k(\boldsymbol{x}+r_{x_i})]\rangle_{xz}}{\langle[u_j(t,\boldsymbol{x})+\widetilde{u}_j(\boldsymbol{x})][u_k(t,\boldsymbol{x})+\widetilde{u}_k(\boldsymbol{x})]\rangle_{xz}}\right)}$$

are displayed in figures 5 and 6. Note that secondary and turbulent fluctuations were sampled together and that the secondary component makes a more 'visual' contribution than the turbulent component. The most noticeable feature of the two-point statistics was the large magnitude of the streamwise correlations for large separations at the rotation rates 0.1 and 0.2. This is most clearly visible in figure 5(*b*)

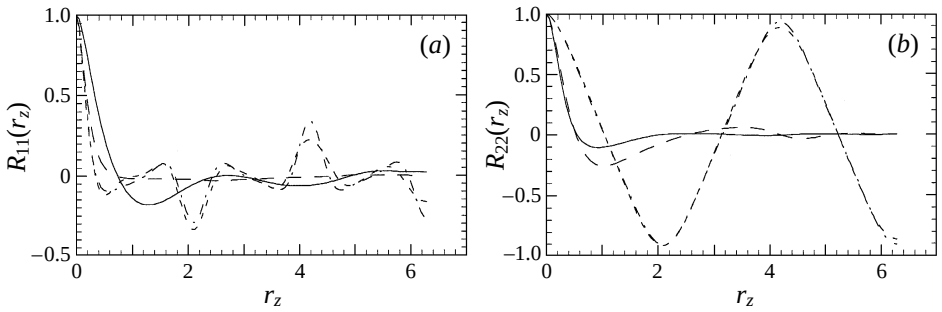

FIGURE 6. Spanwise two-point correlations of (*a*) $u+\widetilde{u}$ and (*b*) $v+\widetilde{v}$ at $y=0$. Legend as in figure 1.

where the wall-normal velocity component is almost fully correlated with itself, i.e. as in laminar flows.

The streamwise correlations of $u+\widetilde{u}$ in figure 5(*a*) attained a lower level than $R_{22}(r_x)$ at large separations for Ro equal to 0.1 and 0.2, indicating that the streamwise component of turbulence was large compared to the wall-normal component at $y=0$. As was shown by BA, streamwise turbulence is produced by the secondary flow, while little energy is transferred from the secondary flow to turbulent fluctuations in the (y,z)-plane.

From $R_{11}(r_z)$ in figure 6(*a*) it can be observed that the variation of the streamwise secondary flow in the z-direction was composed of a periodic variation with wavelength $L_z/3$, i.e. dictated by the computational box, and a harmonic with wavelength $L_z/9$. These wavelengths were more visible in the one-dimensional spectra (not shown). The roll cells observed at weak rotation rates were single-mode, like the roll cell instability in laminar flow computed using linear stability theory, see BA.

The peculiar streamwise oscillations of $R_{11}(r_x)$ at $Ro=0.2$ indicate that some wavy instability, similar to that found by Clever & Busse (1992) in laminar flow, exist also in the turbulent case. By phase-averaging the instantaneous flow field at this rotation rate, using the wavelength $5.28h$ obtained from $R_{11}(r_x)$ and the spanwise wavelength of the roll cells, it was possible to recognize the oscillations in $R_{11}(r_x)$ as a periodic streamwise variation of the secondary flow. By considering a phase-averaged roll cell pair (not displayed here), it became evident that the cross-sectional extent varied and that the flow towards the wall between the counter-rotating vortices exhibited an oscillating spanwise component. Thus the flow pattern was similar to the wavy instability described by Clever & Busse (1992).

In the cases where roll cells were practically absent, i.e. for zero rotation and $Ro=0.5$, an 'inter-component exchange' of streamwise lengthscale was observed. By comparing these two rotation rates in figures 5(*a*) and (*b*), one observes that the lengthscale of the wall-normal velocity fluctuations increased with rotation, while the lengthscale of the streamwise velocity fluctuations decreased. The correlation curves for $Ro=0$ and $Ro=0.5$ are observed to interchange roles, and the same tendency can, to some extent, be observed in figure 6. Thus, due to strong system rotation there seems to be an ordering of the flow structures with significant y-directed momentum, and conversely, break-up into smaller scales of flow structures with significant streamwise momentum. In both cases, however, the plane Couette flow seems to promote flow structures with a strong degree of streamwise coherence, so that the dimensionality (concerning axes) is moderately influenced by rotation, while the componentality (concerning components of velocity and vorticity) is more

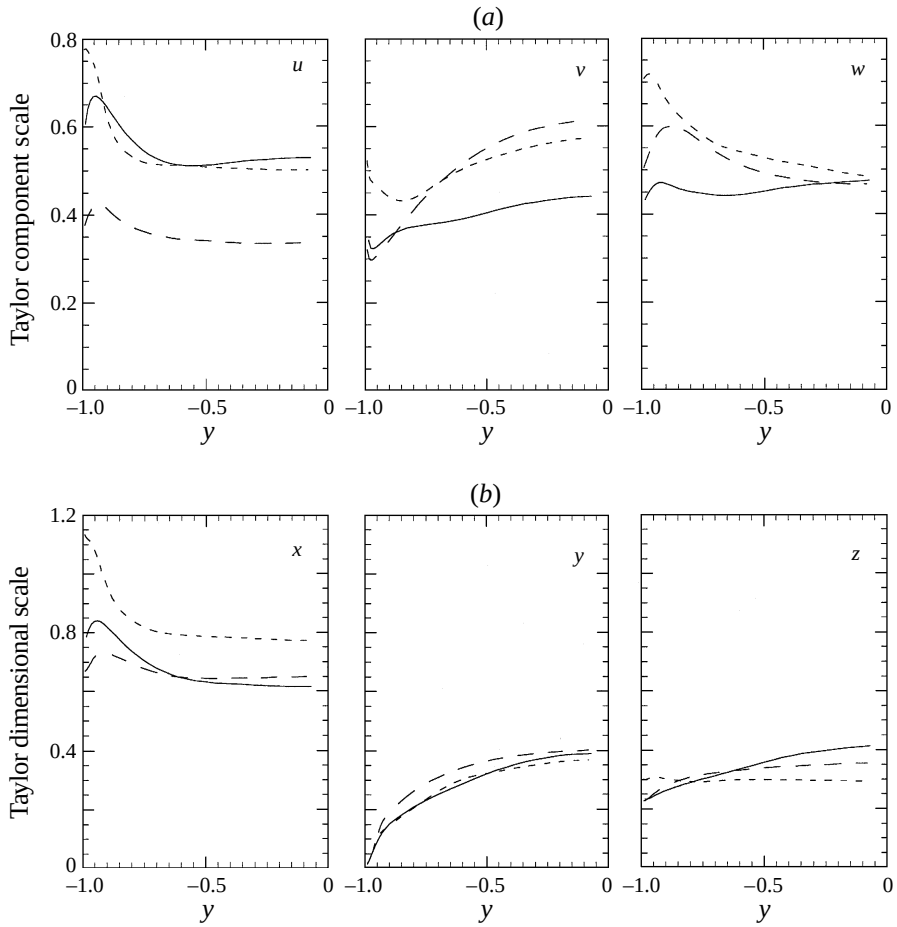

FIGURE 7. Taylor (*a*) component scale and (*b*) directional scale derived from turbulence statistics. Legend as in figure 1.

severely affected. This subject will be further discussed in the next subsection, where turbulence anisotropy is considered.

The conventional definition of the Taylor microscale, as given by for example Tennekes & Lumley (1972), is based on the assumption of isotropic small-scale turbulence. Because system rotation tends to change the *anisotropy* of turbulence, we calculated the Taylor microscale as a tensorial quantity. We stress that we applied turbulent quantities to calculate the lengthscales, so that they are different from those that can be deduced from figures 5 and 6. The component λ_{11}, where $\lambda_{11}^2\langle\overline{(\partial u/\partial x)^2}\rangle_z = \langle\overline{u^2}\rangle_z$, follows the conventional definition of the Taylor microscale. Similarly, we can compute the component $\lambda_{ij} = (\langle\overline{u_i^2}\rangle_z/\langle\overline{(\partial u_i/\partial x_j)^2}\rangle_z)^{1/2}$, *no summation*, where the first index refers to the velocity component, and the latter to the direction of the derivative. A 'Taylor component scale' λ_{u_i} can now be defined, for example by contracting $\lambda_u = (\lambda_{1j}\lambda_{1j})^{1/2}$. These vector components are called component scale because they are independent of the direction, but depend on the actual (velocity) component. The Taylor component scales are visualized, for three different *Ro*, in figure 7(*a*). It should be commented that the *x*-direction seemed to be the most significant, in the sense that the conventional Taylor microscale λ_{11} behaved qualitatively similarly to λ_u. The

same observation was made for λ_{21} and λ_v, as well as for λ_{31} and λ_w, and can only be due to the fact that streamwise gradients were small as a result of elongated turbulent structures.

When discussing the results in figure 7(*a*), one should first of all distinguish between the wall region and the central region. For λ_u, it is readily observed that the scale was significantly shorter at the highest rotation rate. This observation is consistent with figure 5(*a*). The reduction of the lengthscale of the streamwise fluctuations is thus observed to occur everywhere in the channel. It is notable that the lengthscales were similar for zero rotation and $Ro = 0.1$ even though there were large differences with respect to the kinetic energy and the large-scale field. The larger scales were present close to the wall, indicating the existence of low-speed streaks and quasi-streamwise vortices.

The middle diagram of figure 7(*a*) shows λ_v, and again we observe that the lengthscale of the wall-normal fluctuations at $Ro = 0.5$ was much larger than at zero rotation away from the wall. Again, if λ_u and λ_v are compared, the curves for the two rotation numbers zero and 0.5 interchange roles in the central region. The curve for $Ro = 0.1$ approximately follows the largest of the two in all three diagrams of figure 7(*a*). The lower values for λ_v close to the walls were a consequence of damping of wall-normal motions. The last lengthscale is λ_w, which is quite interesting because the velocity component involved, w, is parallel with the axis of rotation and thus affected only indirectly by the Coriolis acceleration. Turbulent fluctuations in the z-direction are sustained by pressure–strain correlations, so that the intensity of this motion should be quite independent of whether $\langle\overline{v^2}\rangle_z$ is smaller or larger than $\langle\overline{u^2}\rangle_z$, i.e. the rotational-induced anisotropy should be of little importance. On the other hand, system rotation can alter the structure of turbulence, which again would affect λ_w. From the figure it is seen that non-zero system rotation tends to generate longer scales, except close to the centreline. In the immediate vicinity of the wall, the lengthscale is largest for $Ro = 0.1$, as it was for λ_u and λ_v, which probably can be ascribed to a low magnitude of turbulent vorticity. The relatively large increase in λ_w close to the wall, from zero rotation to $Ro = 0.5$, is quite surprising after studying the behaviour of λ_u and λ_v. There seems to be an ordering of the spanwise motion along the walls. Around say $y = -0.75$, λ_w follows λ_v rather than λ_u if we compare $Ro = 0.5$ with zero rotation. Thus the increase of λ_v was partly accompanied by an increase in the lengthscale λ_w of the w fluctuations, while the decrease in the lengthscale for the u fluctuations was less influential on λ_w. These observations are consistent with the ordering and intensification of streamwise vorticity observed by Lamballais *et al.* (1996*a*).

It is also possible to compute a 'Taylor directional scale', for example $\lambda_x = (\lambda_{j1}\lambda_{j1})^{1/2}$. Here, the componentality is eliminated by summing over all velocity components or normal stresses, while the directionality is retained. We have visualized the directional scales in figure (7*b*). Considering λ_x, we observe that elongated coherent motions were responsible for large lengthscales close to the walls. This effect was weaker at the highest rotation rate. This may be due to distortion, by the system rotation, of the streaky structures containing streamwise momentum. In the central region, however, λ_x is similar in the cases with zero and maximum rotation. The large x-wise lengthscale for $Ro = 0.1$ seems to indicate a weak x-dependence due to the roll cells, but also a low effective Reynolds number. For λ_y, there are small variations, presumably due to the restrictions on the flow imposed by the solid walls. However, the structures seem to be somewhat more uniform at the highest rotation rate.

In the z-direction, turbulence is homogeneous, while the secondary flow component is periodic. λ_z is observed to behave quite oppositely as compared to λ_x, at least away from the wall. The z-direction is of special interest here, because the Taylor–

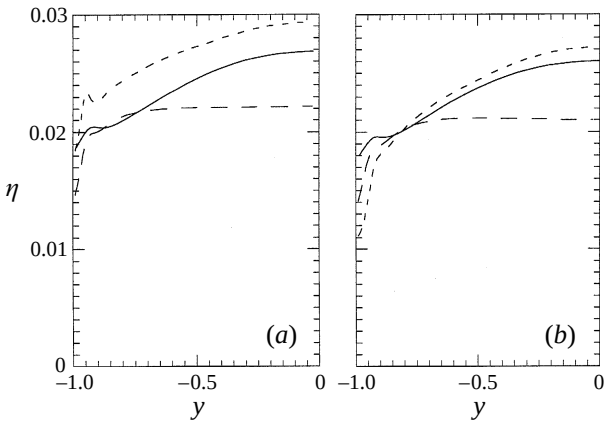

FIGURE 8. Kolmogorov (*a*) turbulent scale and (*b*) turbulent + secondary scale. Legend as in figure 1.

Proudman theorem predicts that the flow field becomes independent of this direction in the limit of infinitely high rotation. Obviously, the rotation rate $Ro = 0.5$ is too low for application of this theorem. Besides, if the flow were to become two-dimensional, then it would also relaminarize. (This occurred when Ro was increased to 1.0 in the present study, but the limit for relaminarization is probably somewhat lower than 1.)

There are, at least, two scalings for the small-scale motions. In channel flow, we usually apply the wall scaling, using friction velocity u_τ and viscosity ν. The half-channel width, measured in these units, is identical to Re_τ given in table 1. The Kolmogorov scale for length, $\eta = (\nu^3/\epsilon)^{1/4}$, where ϵ is the dissipation rate of turbulent kinetic energy, is less frequently used in channel flow applications. In the case of rotation, however, it is of interest to investigate the effect on the lengthscale of the dissipative eddies. In figure 8, both the turbulent (*a*) and total (*b*) dissipation were applied to calculate the Kolmogorov scale. The only significant difference between the two diagrams was associated with the curves for $Ro = 0.1$. By including the secondary dissipation, the Kolmogorov scale decreased significantly, especially very close to the wall. Here, the roll cells created high shear rates and thus increased the dissipation. By including the secondary dissipation, however, the Kolmogorov lengthscale loses some of its physical meaning because the secondary motion was large-scale and not cascade-like. We therefore concentrate on figure 8(*a*). For zero rotation and $Ro = 0.1$, the behaviour was qualitatively similar. The roll cells damped the turbulence and increased the Kolmogorov lengthscale. The dissipation rate was high in the immediate vicinity of the walls, and decreased towards the centreline. At $Ro = 0.5$, the Kolmogorov scale illustrates an important point, namely the high and almost uniform dissipation rate throughout a substantial portion of the channel. This behaviour is qualitatively different from the two other cases and can be associated with the relatively high magnitude, as well as the approximate constancy, of the mean shear, clearly shown in figure 1.

4.3. *Enstrophy and kinetic energy*

The variation of the r.m.s. vorticity (the square root of twice the enstrophy) across the channel is shown in figure 9. The turbulent enstrophy follows the same trend from the centreline and towards the wall in the cases with $Ro \leqslant 0.2$. The decrease observed in the central region, when Ro was increased from zero to 0.1, was caused

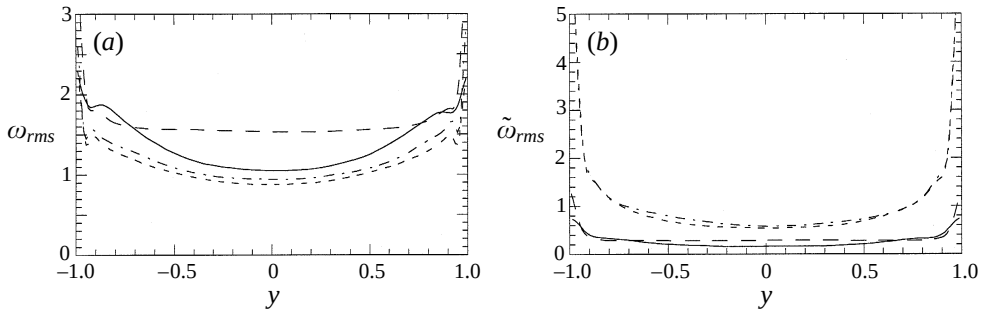

FIGURE 9. R.m.s. vorticity: (*a*) turbulent, and (*b*) secondary. Legend as in figure 1.

by damping of the x- and z-components† of vorticity. The increased level of turbulent enstrophy at $Ro = 0.5$ was caused by a substantial growth of the x-directed vorticity. The approximate constancy of the enstrophy in a large portion of the flow could be recognized in all three components and can be associated with the high, almost uniform shear rate observed at $Ro = 0.5$. The approximate constancy of the vorticity at $Ro = 0.5$ was observed indirectly in figures 7 and 8. The behaviour of the secondary r.m.s. vorticity depicted in figure 9(*b*) reflects the relative importance of the secondary flow at $Ro = 0.1$ and 0.2. At these rotation rates, the secondary vorticity exhibited high values at the wall due to both the streamwise and spanwise components. The r.m.s. secondary wall shear-stress gave a friction velocity that was 70% of the total u_τ. In the core region, the growth of secondary enstrophy was caused by the x- and y-components, while the z-directed secondary vorticity was approximately unaltered by rotation.

Figure 10 displays an anisotropy invariant map (AIM, see Lumley 1978) for the turbulent vorticity tensor

$$v_{ij} = \frac{\langle\overline{\omega_i\omega_j}\rangle_z}{\langle\overline{\omega_k\omega_k}\rangle_z} - \frac{\delta_{ij}}{3}, \tag{4.1}$$

at two different y-values. The second and third invariants are

$$\mathrm{II} = \frac{1}{2}\left(v_{ii}v_{jj} - v_{ii}^2\right), \quad \mathrm{III} = \frac{1}{3!}\left(v_{ii}v_{jj}v_{kk} - 3v_{ii}v_{jj}^2 + 2v_{ii}^3\right). \tag{4.2}$$

Note that v_{ii}^2 and v_{ii}^3 denote the traces of $v_{ij}^2 = v_{ik}v_{kj}$ and $v_{ij}^3 = v_{ik}v_{kl}v_{lj}$, respectively. Close to the walls, there seems to be a trend towards increasing isotropy with increasing rotation rate. At $Ro = 0$, the vorticity tensor was approximately axisymmetric, with the z-component significantly larger than the other two. (Here, it should be noted that one-component vorticity and two-component velocity may typically coincide. It is a bit more difficult to imagine axisymmetric vorticity than axisymmetric velocity.) The main effect of increasing the rotation number to 0.1 was to increase the streamwise component relative to the other components of vorticity, thereby departing from axisymmetry, and also from one-componentality. By further increasing the rotation rate to $Ro = 0.5$, the growth of the streamwise component made it approximately equal to the z-component which was slightly damped, i.e. the vorticity became approximately axisymmetric, with one component (y) smaller than the others. In summary, the effect of system rotation in the near-wall region was to increase the streamwise component and to slightly decrease the spanwise component of turbulent vorticity.

† By x-component of vorticity we mean the r.m.s. of ω_x or the 11-component of the vorticity tensor $\langle\overline{\omega_i\omega_j}\rangle_z$.

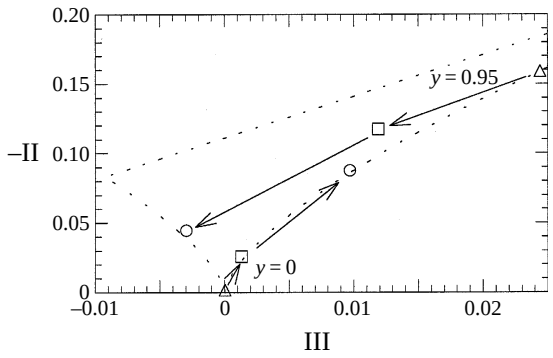

FIGURE 10. AIM for the turbulent vorticity tensor $\langle\overline{\omega_i\omega_j}\rangle_z$. △, $Ro = 0$; □, $Ro = 0.1$; ○, $Ro = 0.5$. The points along the upper line are averages for $y = \pm 0.95$.

The behaviour of the vorticity anisotropy at the centreline $y = 0$ was quite different and one can readily observe a departure from isotropy, or even an 'inverse return to isotropy'. If one were to imagine that the rotation number was suddenly decreased from 0.5 to zero, the path† followed by the vorticity anisotropy would resemble that derived from return-to-isotropy simulations of homogeneous turbulence after removal of the mean shear, see Lee & Reynolds (1985). Both high mean shear as well as strong system rotation represent distortions to the turbulent flow field that increase the anisotropy of the vorticity tensor. A significant change induced by increasing the rotation rate from zero to 0.1 was, as shown in figures 4 and 9(*a*), to damp the turbulent enstrophy. There was, however, an increase in the y-component of vorticity which made the vorticity tensor more anisotropic. From figure 9(*a*) it is known that the turbulent r.m.s. vorticity at $y = 0$ was at least 50% larger at $Ro = 0.5$ as compared to the other rotation numbers. If we compare the two rotation numbers 0 and 0.5, the tendency towards axisymmetry with one leading component at $Ro = 0.5$ was due to an approximate doubling of the streamwise r.m.s. vorticity.

The kinetic energy of turbulence is depicted in figure 11(*a*) and the secondary kinetic energy in figure 11(*b*). At weak rotation rates (0.01, treated in BA), the near-wall peaks in k, characteristic of non-rotating near-wall flows, were clearly visible. These peaks were due to the maxima in $\langle\overline{u^2}\rangle_z$, and disappeared at higher rotation rates. As discussed above, the turbulent kinetic energy was lowest when $Ro \sim 0.1$. (It should be remarked that the turbulent shear stress $-\langle\overline{uv}\rangle_z$ became negative around $y = \pm 0.6$ in this case.) The almost uniform level of k for $Ro \sim 0.1$ was due to significant secondary production of $\langle\overline{u^2}\rangle_z$ as discussed in BA. The growth of the turbulent kinetic energy when Ro was increased from 0.2 to 0.5 took place in the central region of the flow and was due to the growth in $\langle\overline{v^2}\rangle_z$, which is plotted in figure 12. The disappearance of the roll cells was associated with a substantial increase in $\langle\overline{v^2}\rangle_z$ in the central region, which caused the change of the distribution of k in figure 11(*a*).

The kinetic energy $\widetilde{k}$ associated with the secondary flow exhibited peaks in the near-wall region at $Ro = 0.1$ and 0.2 and resembled k in the non-rotating case, i.e. the streamwise component $\langle\tilde{u}^2\rangle_z$ was large compared to $\langle\tilde{v}^2\rangle_z$ and $\langle\tilde{w}^2\rangle_z$ and exhibited maxima in the near-wall regions. The very high intensity of the secondary flow was due to the mixing by the regular roll cells, combined with high shear (figure 1), and

† We only have access to 3 discrete points on this 'path'.

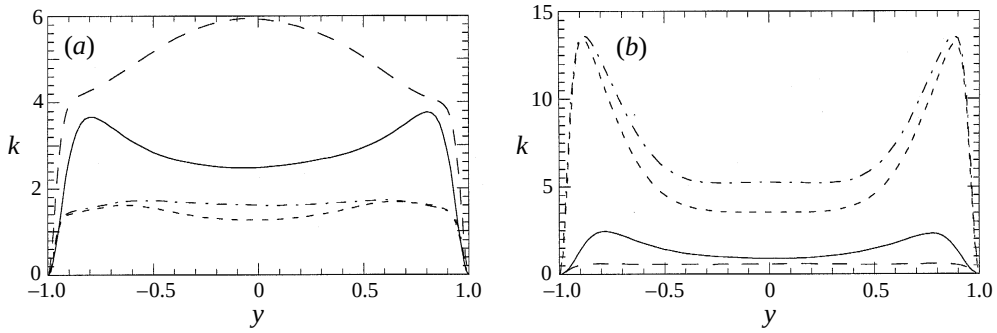

FIGURE 11. Kinetic energy: (*a*) k (turbulent); (*b*) $\widetilde{k}$ (secondary). Legend as in figures 1 and 2. $Ro = 0$ is not shown.

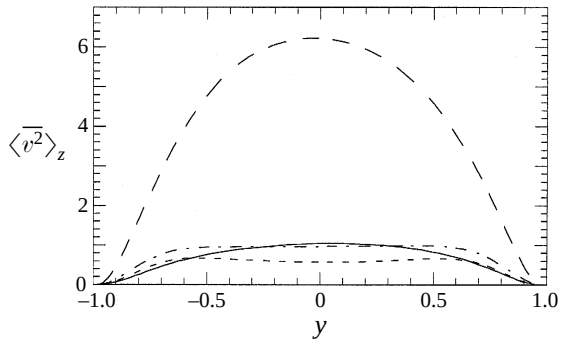

FIGURE 12. $\langle\overline{v^2}\rangle_z$. Legend as in figure 11.

exceeded the intensity of the turbulent motion. If we consider the change in $k+\widetilde{k}$ when Ro is increased from 0.2 to 0.5, we observe a small decrease at the centreline (about 5%) and a large decrease (up to about 70%) closer to the walls. It is evident that ordered structures like the secondary flow are able to maintain more energetic motion than turbulence, and that these motions, at least partially, disappeared when Ro was increased to 0.5. The energy distributions of figure 11 exhibit the two different flow regimes induced by strong rotation observed in this study, and it is obvious that the differences between these two regimes are not caused by the present decomposition and averaging technique, because the differences would still be clearly visible in a plot of $k+\widetilde{k}$.

4.4. *Rotational effects on near-wall turbulence-generating events*

Before considering the conditional averages, we will discuss time-averaged contributions to the total shear stress $-\langle\overline{uv}+\tilde{u}\tilde{v}\rangle_z$ from the quadrants in the $(u+\tilde{u}, v+\tilde{v})$-plane. Time-averaged results do not suffer from the 'subjectivity' of conditional averages, and they are thus a good starting point for the analysis. We have made a comparison between the quadrant analysis of the present Couette flow and Poiseuille flow simulations by Kristoffersen & Andersson (1993) at $Re = 2900$, with and without system rotation, in figure 13. The results for Poiseuille flow at $Ro = 0.5$, where the rotation number is based on the bulk mean velocity, are previously unpublished data. In the diagram, no distinction is made between the secondary and turbulent components of the velocity fluctuations. As discussed above, the secondary component was probably a by-product of the finite computational domain at these rotation rates and thus of

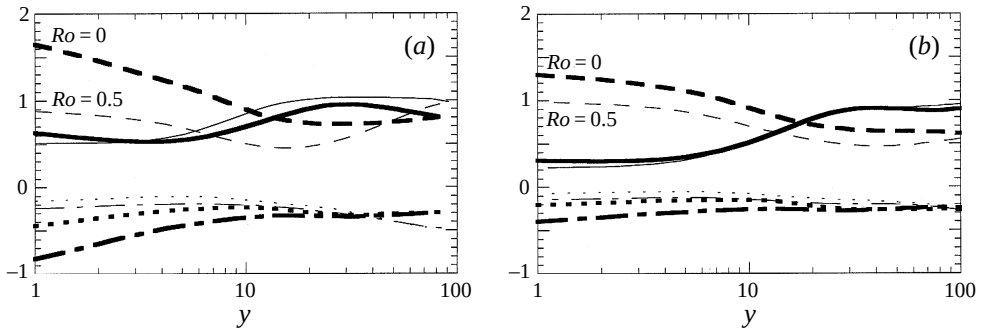

FIGURE 13. Fractional contributions to the shear-stress $\langle \overline{uw} + \widetilde{uw} \rangle_z$ at two different rotation rates. (*a*) present Couette flow, (*b*) the Poiseuille flow simulations by Kristoffersen & Andersson (1993). Bold lines: $Ro = 0$, thin lines: $Ro = 0.5$. — - —, Q1($u > 0, v > 0$); —, Q2($u < 0, v > 0$); - - -, Q3($u < 0, v < 0$); — — —, Q4($u > 0, v < 0$).

Ro	n_{Q2}	n_{Q4}	Re_τ	Re_t
0.0	0.25	0.22	82.2	142.4
0.1	0.12	0.19	106.7	97.6
0.5	0.26	0.14	91.0	180.9

TABLE 3. Number of Q2 and Q4 detections per unit area (made dimensionless with h^2).

little significance in the case of Couette flow. Kristoffersen & Andersson observed splitting and merging roll cells at $Ro = 0.5$, so that their results for the shear stress at $Ro = 0.5$ may have had a significant secondary component.

Figure 13 shows that the contribution from quadrant 2 (Q2, ejections) events was only marginally influenced by rotation in the case of Poiseuille flow. The same tendency can be seen in the Couette flow. Note that the contributions from Q2 and Q4 must be equal at the centreline in the case of Couette flow due to the antisymmetry of the mean velocity distribution. Shifting the attention to the fourth quadrant, we observe the most striking effect of system rotation, namely a substantial reduction of the relative importance of Q4 events (sweeping motions). There was also a significant decrease in the (negative) contribution from Q1 events, which, to some extent, can be considered as the outcome of sweeps being reflected by the wall.

Detection of Q2 and Q4 events was carried out at the three rotation numbers 0, 0.1 and 0.5. The ensemble averages to be discussed in this section was obtained using the detection method described in §3. After detecting the sweeps and ejections, the maximum of the turbulent shear stress in each event was found. The coordinate system of each event was translated to make the origin coincide with this maximum before the events were ensemble averaged. There were, of course, two sets of ensemble averages, one for Q2 and one for Q4 (The ensemble average of e.g. u with respect to Q2 detection is denoted by $\langle u \rangle_{Q2}$). Between 300 and 600 presumably independent events of each kind were detected at the non-zero rotation numbers. At zero rotation, the time increment between the fields in the database was about one half of that applied in the other two cases, but the number of detections was similar. The number of events detected, divided by the size of the (x, z)-plane, is tabulated in table 3, while the sampling time was given in table 1 ($T_{s,2}$). The modest number of Q4 detections at $Ro = 0.5$ is in accordance with the time-averaged statistics displayed in figure 13. The

relatively few events detected at $Ro = 0.1$ could be a result of strong secondary flow and suppression of turbulence. It is not likely that the threshold value for detection, discussed in §3, was too high. At $Ro = 0.1$, a great deal of the turbulence production was caused by secondary shear (for example $\partial\tilde{u}/\partial z$) in the core region, cf. figure 11*(a)*, so that the near-wall region was of less relative importance. In both cases of non-zero rotation, the number of detections was reduced as compared to $Ro = 0$. Even if the volume-averaged turbulent kinetic energy attained its maximum at $Ro = 0.5$, the energy was differently distributed (see §4.3), so that less turbulence was produced in the near-wall region.

To visualize the kind of events detected and the primary effect of the Coriolis acceleration, cross-sections through the ensemble averages at $z = 0$ are presented in figure 14 for Q2 events and in figure 15 for Q4 events. The Coriolis acceleration made the v-component relatively more important, as can be inferred from the direction of the velocity vectors. The angle between the velocity vector at the detection point and the wall was approximately doubled for both sweeps and ejections when Ro was increased from 0 to 0.5. At $Ro = 0.1$, the events seem to be confined to a thin layer near the wall, presumably due to squeezing by the roll cells. For $Ro = 0.5$, the events exhibited higher shear near the wall, and the region of streamwise motion was shortened as compared to the $Ro = 0$ case. Away from the wall, the v-component was relatively more important than in the non-rotating case so that the y-directed motion, as visualized by the velocity vectors, was clearly visible at the centreline $y = 0$ in the case of $Ro = 0.5$. Evidently, the events were responsible for a larger transport of momentum across the centreline, i.e. the size, as well as the intensity, of the cross-flow eddies were increased.

After inspection of several cross-sections in various directions of the ensemble averages of the different flow variables, it became evident that the most significant differences were found when the Q2 ensemble average at $Ro = 0.5$ was compared with the non-rotating case. In the following, a few of a very large number of possible visualizations will be displayed, and we have chosen to concentrate on the streamwise vorticity. In figures 16 and 17, a comparison is made between visualizations of velocity vectors in the cross-flow plane for Q2 events. In figure 16(*a–d*), the wall ($y = -1$) is located at the bottom and the view extends to the centreline at $y = 0$. In figure 17, the entire cross-section is shown from the lower to the upper wall. In the non-rotating case one can observe the typical streamwise vortex on the right-hand side of the ejection. Similar diagrams can be found in Guezennec *et al.* (1989) and Nishino & Kasagi (1991), while a discussion can be found in Bech *et al.* (1995). Upstream of the detection point, in figure 16(*a*), spanwise motion generates a vortex close to the wall. Downstream the vortex axis points away from the wall and forms an angle with the streamwise axis. Further downstream, the vortex became practically invisible. The spanwise lengthscale of the vortex in figure 16 was approximately the same as in the two studies cited above. Nishino & Kasagi suggested a streamwise lengthscale of 300 wall units. In the present study, we found that this lengthscale was closer to 250 wall units by considering contour plots of ensemble-averaged streamwise vorticity.

Turning our attention to the ensemble average at $Ro = 0.5$ in figure 17, we observe that although the qualitative behaviour is similar to that for $Ro = 0$, some significant differences are visible. Upstream of the detection point, a large-scale vortex is observed at the left-hand side. This vortex can be followed downstream, and is actually longer than the ejection vortex at the right-hand side. It is notable that the vortex was fairly undistorted and that its axis was almost parallel to the x-axis. This is in agreement with the recent finding of Lamballais *et al.* (1996*a*). Likewise, the ejection vortex,

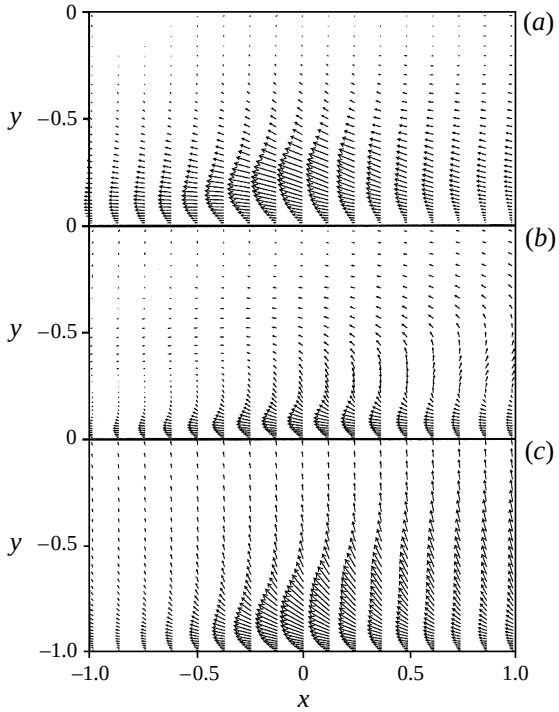

FIGURE 14. Ensemble-averaged velocity vectors $(\langle u\rangle_{Q2}, \langle v\rangle_{Q2})$ for Q2 events in the plane $z = 0$. (*a*) $Ro = 0$; (*b*) $Ro = 0.1$; (*c*) $Ro = 0.5$. Same vector scaling applied in all plots. The detection was carried out near the lower wall at $y = -1$, only the lower half-channel is shown.

clearly visible in figure 17(*b*), seems to be relatively stable. The final picture 17(*f*) is quite similar to a roll cell pair. However, the intensity of this vortical motion was an order of magnitude smaller than the intensity of the secondary motion at $Ro = 0.1$. Corresponding visualizations of the Q4 ensemble average showed that the sweeps were associated with significant streamwise vorticity for $Ro = 0.5$, but the streamwise lengthscale was significantly smaller than what was the case for Q2 events. Thus, the rotational effect on the sweeps was less pronounced.

Consider the rotation number based on the conditionally averaged vorticity, i.e. $\langle Ro\rangle_{Qn} = -2\Omega/(W + \langle\omega_z\rangle_{Qn})$, where n can be 2 or 4. In the interval $y < -0.4$, $\langle Ro\rangle_{Q4}$ was greater than unity while $\langle Ro\rangle_{Q2}$ was less than unity so that only Q2 events can be said to be in the destabilized range. A further observation was that the conditionally averaged vorticity $\langle\omega_z\rangle_{Qn}$ was anticyclonic in the case of $n = 2$ and cyclonic in the case of $n = 4$. Thus, the relatively low impact of the sweeps can be a result of local stabilization The large streamwise lengthscales exhibited by the Q2 events, and not the Q4 events, at the highest rotation rate are in agreement with the observations of Bartello *et al.* (1994), i.e. anticyclonic two-dimensional structures are stretched in the longitudinal direction while the cyclonic structures are not.

5. Final discussion and conclusions

The evaluation of the results from simulations of rotating turbulent plane Couette flow is not straightforward because of the lack of experimental data and other numerical simulations. We have, however, verified our results for the non-rotating

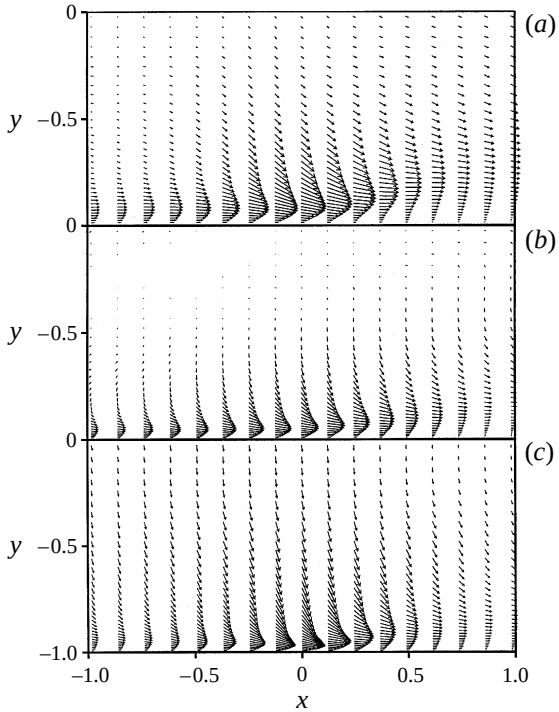

FIGURE 15. As figure 14 but for Q4 events.

turbulent case as well as the laminar rotating case. In Bech *et al.* (1995) it was observed that the near-wall turbulence was in agreement with available results from plane Poiseuille flow. The latter point is interesting, and supports the use of experimental and numerical results from the rotating turbulent plane Poiseuille flow for comparative purposes.

The consistency of the simulations with rotation can be evaluated on the basis of rotational effects on the laminar flow configuration, i.e. the roll cell instability and also the wavy instability, and the analogous effects on the Poiseuille flow (observed on the anticyclonic side). The roll cell instability occurs in linear stability analysis of the rotating laminar plane Couette flow, and the occurrence of such structures in the turbulent case was therefore physically plausible. The breakup of the two-dimensional roll cells into three-dimensional wavy rolls or time-dependent (so-called vacillating) instabilities, has been predicted for the almost analogous Rayleigh–Bénard case by Clever & Busse (1992). DNS of the turbulent Rayleigh–Bénard case by Domaradzki & Metcalfe (1988) showed that the regular streamwise structures broke up at high Rayleigh numbers.

Considering the combined effects on turbulence and roll cells, the present investigation compares favourably with the investigations by Johnston *et al.* (1972) and Kristoffersen & Andersson (1993). In both flows it has been observed that destabilizing system rotation with $Ro \sim 0.01$ resulted in a sudden increase in the intensity of the fluctuating flow field. Similarly, strong system rotation was accompanied by a region of approximately zero absolute vorticity. Roll cells have been observed in both flows, although much more intense in the Couette case. The reinforcement of the wall-normal fluctuations and the attenuation of the streamwise fluctuations due

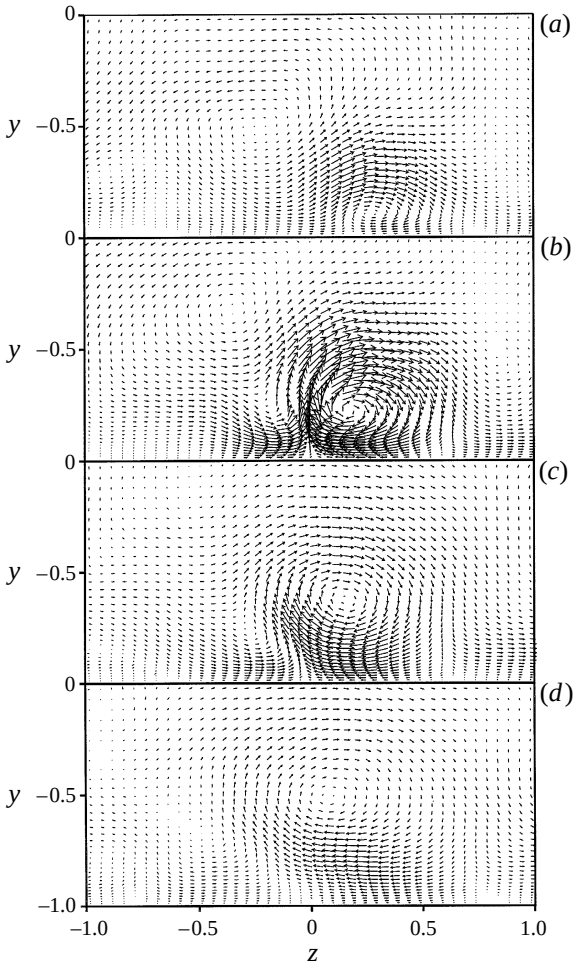

FIGURE 16. $(\langle w\rangle_{Q2}, \langle v\rangle_{Q2})$ in the cross-flow plane at different x-positions at $Ro = 0$. (*a*) $x = -0.61$; (*b*) $x = 0$; (*c*) $x = 0.61$; (*d*) $x = 1.23$.

to destabilizing rotation have been observed in Poiseuille flow as well as Couette flow. Finally, the tendency for system rotation to favour ejecting motions and suppress sweeping motions in the destabilized wall layer has been observed in simulations of both types of flow. Some care must be taken here because rotating Poiseuille flow exhibits both a destabilized and a stabilized side. Thus, total relaminarization, which has to occur on both sides of the centreline, cannot be expected to occur at the same rotation number in the two flows. Also the effect of a certain rotation rate can be different between the two flows.

Both Poiseuille flow and Couette flow exhibited destabilized regions where the anisotropy $a > 0$. These regions with reversal of the anisotropy of the fluctuating flow field (turbulent + secondary) were approximately correlated with regions where $S \sim -1$. It is interesting to note that S could be somewhat less than -1, which is in accordance with the criterion (2.4). The condition of strong rotation, $a > 0$, seems to be sensible for channel flow as long as the region close to the wall is not considered and there are reservations for the region of the Poiseuille flow where the mean vorticity changes sign. The extent of the region with $a > 0$ increased with increasing rotation

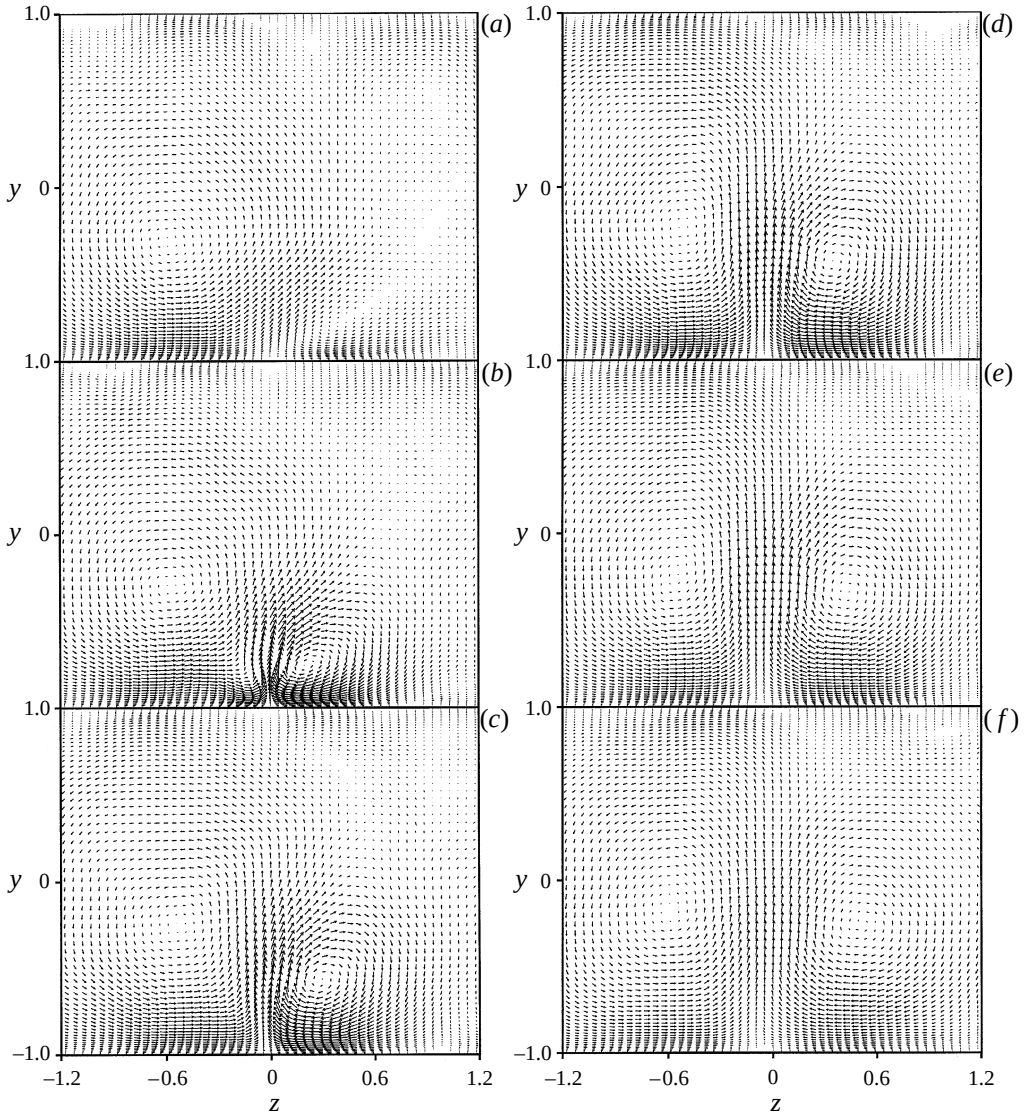

FIGURE 17. ($\langle w\rangle_{Q2}, \langle v\rangle_{Q2}$), $Ro = 0.5$. (*a*) $x = -0.61$; (*b*) $x = 0$; (*c*) $x = 0.61$; (*d*) $x = 1.23$; (*e*) $x = 1.84$; (*f*) $x = 2.45$.

rate, and the existence of such a region was independent of the existence of roll cells, but associated with an ordering and intensifying of the streamwise vorticity.

In all cases with destabilization, the streamwise vorticity was more predominant than in the non-rotating case. Secondary, as well as coherent, streamwise vorticity has been shown to be strongly favoured by anticyclonic system rotation. It is convenient to speak of two different regimes of strong rotation. The first regime was that of roll cells, or secondary streamwise vorticity, high wall shear stress and low turbulence intensity. For practical purposes, mixing and heat conduction will be significantly amplified in this regime. This regime was also observed in the experiments of Tillmark & Alfredsson (1996). The spanwise lengthscale of the roll cells observed by Tillmark & Alfredsson is in perfect agreement with the present results. The roll cells observed

in the turbulent flow are similar to those caused by the Coriolis acceleration in the laminar flow. As observed in the experiments, the roll cells are less prone to three-dimensionalization when the flow is turbulent. The roll cells change shape as they intensify, and become more similar to the roll cells observed in rotating Poiseuille flow in that the most intense motion is associated with fluid ejecting from the wall. Maximum destabilization occurred when the background vorticity was similar to the mean vorticity of the core region in the non-rotating flow, i.e. at $Ro \simeq 0.2$.

The second regime was that of streamwise turbulent vortices originating from the anticyclonic wall layer. In this regime, the wall shear stress and the turbulence intensity was more similar to the non-rotating case. However, the structure of turbulence was significantly altered after the roll cells broke up. Both directionality and dimensionality were different from the conventional channel flow. The dominance of the streamwise vorticity was deduced from both time-averaged statistics and conditional averages. A similar remarkable ordering and intensifying of the streamwise vorticity was observed in rotating Poiseuille flow simulations by Lamballais *et al.* (1996*a*). They observed that the vorticity was generated mainly through the stretching terms in the transport equation for the r.m.s. vorticity. Comparing the second regime with the non-rotating case, it is interesting to observe that the Taylor component scale λ_u decreased, while the Taylor directional scale λ_x did not (at least away from the wall). This was because the long regions of coherent streamwise momentum were partly replaced by coherent streamwise vortices, so that the componentality of the most energetic motion increased from one to two. The distribution of the turbulent motion changed with system rotation so that the relative importance of the central region increased. At the highest rotation rate $Ro = 0.5$, this region exhibited higher mean shear and a broader range of scales of motion as compared to the non-rotating case.

Finally, it is interesting to consider the dimensionality of the mean and secondary flow fields. From linear stability theory, it is known that destabilization is equivalent to a two-dimensionalization of the initially one-dimensional flow. Indeed we observe the same phenomenon in the turbulent Couette flow. Moreover, when the total kinetic energy decreases, i.e. when the flow restabilizes as Ro gets close to 0.5, the two-dimensional secondary flow vanishes. It is obvious that the most significant destabilization is due to the ordering of the flow so that energy is kept in large-scale motions and partly prevented from travelling down the cascade to the dissipative scales. In the case of restabilization, the secondary flow field was observed to three-dimensionalize, i.e. the roll cells broke up in the streamwise direction, and the dissipation increased significantly, thereby reducing the overall kinetic energy.

We are grateful to the referees for their constructive comments. The computing time for the simulations was provided by the Norwegian Supercomputing Committee (TRU).

REFERENCES

Andersson, H. I. & Kristoffersen, R. 1995 Turbulence statistics of rotating channel flow. In *Turbulent Shear Flows 9* (ed. F. Durst, N. Kasagi, B. E. Launder, F. W. Schmidt, K. Suzuki & J. H. Whitelaw), p. 53. Springer.

Bartello, P., Metais, O. & Lesieur, M. 1994 Coherent structures in rotating three-dimensional turbulence. *J. Fluid Mech.* **273**, 1.

Bech, K. H. & Andersson, H. I. 1996*a* Secondary flow in weakly rotating turbulent plane Couette flow. *J. Fluid Mech.* **317**, 195 (referred to herein as BA).

Bech, K. H. & Andersson, H. I. 1996*b* Structure of Reynolds shear-stress in the central region of plane Couette flow. *Fluid Dyn. Res.* **18**, 65.

Bech, K. H. & Andersson, H. I. 1996*c* Growth and decay of longitudinal roll cells in rotating turbulent plane Couette flow. In *Advances in Turbulence VI* (ed. S. Gavrilakis *et al.*), p. 91. Kluwer.

Bech, K. H., Tillmark, N., Alfredsson, P. H. & Andersson, H. I. 1995 An investigation of turbulent plane Couette flow at low Reynolds numbers. *J. Fluid Mech.* **286**, 291.

Bidokhti, A. A. & Tritton, D. J. 1992 The structure of a turbulent free shear layer in a rotating fluid. *J. Fluid Mech.* **241**, 469.

Bradshaw, P. 1969 The analogy between streamline curvature and buoyancy in turbulent shear flow. *J. Fluid Mech.* **36**, 177.

Cambon, C., Benoit, J.-P., Shao, L. & Jacquin, L. 1994 Stability analysis and large-eddy simulation of rotating turbulence with organized eddies. *J. Fluid Mech.* **278**, 175.

Clever, R. M. & Busse, F. H. 1992 Three-dimensional convection in a horisontal fluid layer subjected to a constant shear. *J. Fluid Mech.* **234**, 511.

Domaradzki, J. A. & Metcalfe, R. W. 1988 Direct numerical simulation of the effects of shear on turbulent Rayleigh-Benard convection. *J. Fluid Mech.* **193**, 499.

Gavrilakis, S., Tsai, H. M., Voke, P. R. & Leslie, D. C. 1986 Large-eddy simulation of low Reynolds number channel flow by spectral and finite difference methods. In *Notes on Numerical Fluid Mechanics* (ed. U. Schumann & R. Friedrich), vol. 15, p. 105. Vieweg.

Greenspan, H. P. 1968 *The Theory of Rotating Fluids.* Cambridge University Press.

Guezennec, Y. G., Piomelli, U. & Kim, J. 1989 On the shape and dynamics of wall structures in turbulent channel flow. *Phys. Fluids* A **1**, 764.

Hart, J. E. 1971 Instability and secondary motion in rotating channel flow. *J. Fluid Mech.* **45**, 341.

Johnston, J. P., Halleen, R. M. & Lezius, D. K. 1972 Effects of spanwise rotation on the structure of two-dimensional fully developed turbulent channel flow. *J. Fluid Mech.* **56**, 533.

Komminaho, J., Lundbladh, A. & Johansson, A. V. 1996 Very large structures in plane turbulent Couette flow. *J. Fluid Mech.* **320**, 259.

Koyama, H. S. & Ohuchi, M. 1985 Effects of Coriolis force on boundary layer developement. In *Proc. 5th Symp. on Turbulent Shear Flows, Ithaca*, pp. 21.19–21.24.

Kristoffersen, R. & Andersson, H. I. 1993 Direct simulations of low-Reynolds-number turbulent flow in a rotating channel. *J. Fluid Mech.* **256**, 163.

Lamballais, E., Lesieur, M. & Metais, O. 1996*a* Influence of a solid-body rotation upon coherent vortices in a channel. *C.R. Acad. Sci. Paris* **323**, II*b*, 95.

Lamballais, E., Lesieur, M. & Metais, O. 1996*b* Effects of spanwise rotation on the vorticity stretching in transitional and turbulent channel flow. *Intl J. Heat Fluid Flow* **17**, 324.

Lee, M. J. & Reynolds, W. C. 1985 Numerical experiments on the structure of homogeneous turbulence. Rep. TF-24. Department of Mechanical Engineering, Stanford University.

Lesieur, M., Yanase, S. & Metais, O. 1991 Stabilizing and destabilizing effects of solid-body rotation on quasi-two-dimensional shear layers. *Phys. Fluids* A **3**, 403.

Lumley, J. L. 1978 Computational modeling of turbulent flows. *Adv. Appl. Mech.* **18**, 123.

Metais, O., Flores, C., Yanase, S., Riley, J. J. & Lesieur, M. 1995 Rotating free-shear flows. *J. Fluid Mech.* **293**, 47.

Metais, O., Yanase, S., Flores, C., Bartello, P. & Lesieur, M. 1992 Reorganization of coherent vortices in shear layers under the action of solid-body rotation. In *Turbulent Shear Flows 8*, p. 415. Springer.

Nakabayashi, K. & Kitoh, O. 1996 Low Reynolds number fully developed two-dimensional turbulent channel flow with system rotation. *J. Fluid Mech.* **315**, 1.

Nishino, K. & Kasagi, N. 1991 On the quasi-coherent turbulence structures in the two-dimensional channel flows. In *Proc. 8th Symp. on Turbulent Shear Flows, Munich*, Paper 28-3.

Tafti, D. K. & Vanka, S. P. 1991 A numerical study of the effects of spanwise rotation on turbulent channel flow. *Phys. Fluids* A **3**, 642.

Tennekes, H. T. & Lumley, J. L. 1972 *A First Course in Turbulence.* MIT Press.

Tillmark, N. & Alfredsson, P. H. 1996 Experiments on rotating plane Couette flow. In *Advances in Turbulence VI* (ed. S. Gavrilakis, *et al.*), p. 391. Kluwer.

Tritton, D. J. 1992 Stability of turbulent shear flow in a rotating fluid. *J. Fluid Mech.* **241**, 503.